

ARTICLE OPEN



Smart coating with dual-pH sensitive, inhibitor-loaded nanofibers for corrosion protection

Chao Li¹, Xiaolei Guo¹ and Gerald S. Frankel¹✉

Smart coatings that provide corrosion protection on demand have received a lot of recent attention. In the present study, nanofibers containing a corrosion inhibitor were prepared by a coaxial electrospinning technique, which addresses the limitations of inhibitor-loaded microcapsules or nanocontainers. The as-prepared nanofibers have a core-shell structure with Ce(NO₃)₃ and the chitosan/polyacrylic acid polyelectrolyte coacervate as the core and shell materials, respectively. UV-vis spectroscopic analysis confirms that the nanofibers are pH-sensitive and able to release the enclosed Ce(NO₃)₃ at both low and high pH conditions, which are spontaneously generated during corrosion at local anodes and cathodes, respectively. A coating system consisting of such nanofibers within a polyvinyl butyral coating matrix exhibits improved corrosion protection of an AA2024-T3 substrate. Moreover, the embedded Ce(NO₃)₃-loaded nanofibers can persistently release Ce(NO₃)₃ to impede corrosion of AA2024-T3 when the artificially damaged coating sample is exposed to NaCl solution.

npj Materials Degradation (2021)5:54; <https://doi.org/10.1038/s41529-021-00203-3>

INTRODUCTION

Aluminum alloys, including AA2024-T3, are strong and light aerospace-grade materials but they suffer from localized corrosion mainly due to the microgalvanic coupling between the inter-metallic particles and the aluminum matrix¹. Coatings with corrosion inhibitors have been widely used to protect these alloys from corrosion^{2,3}. For instance, inhibitive pigments such as strontium chromate, lithium carbonate, and cerium cinnamate are directly introduced into the coating matrix to obtain the desired protectiveness in harsh environments^{4–6}. However, these active inhibitors may detrimentally affect the barrier property of the coating and be quickly depleted by uncontrolled leaching^{7,8}. To address these issues, inhibitors can be confined within micro or nano capsules. A major benefit of using capsules is to isolate inhibitive species from the polymeric coating matrix, so the adverse interactions can be minimized^{9,10}. Additionally, the shell of these capsules can serve as a diffusion barrier to prevent the uncontrolled release of corrosion inhibitors, avoiding the rapid depletion of inhibitors and ensuring corrosion protection performance for extended periods¹¹. Despite their advantages, the capsules also have notable limitations such as undermining the integrity of the coating matrix¹². When these capsules are impregnated within a coating, new interfaces between the capsules and the coating matrix are produced. This may lead to the generation of defects at the interfaces or induce local stress concentration, threatening the structural stability of the coating^{12,13}. Moreover, the heterogeneous distribution of inhibitor-loaded capsules within the coating evidently affects the supply of corrosion inhibitors in different locations^{14,15}. This may result in low corrosion inhibition efficacy in the areas where fewer inhibitor-loaded capsules are present. Additionally, these capsules are discretely embedded within the coating^{14,16}, so it is difficult to replenish the corrosion inhibitors after they are released. As a result, the continuous protection of metals against corrosion for extended periods is not guaranteed.

To overcome the issues mentioned above, an alternative approach based on manufacturing nanofibers has attracted

increasing attention recently. Due to the presence of interfibrillar pores, the intrusion of the coating matrix solution into the nanofiber network can be facilitated, thus interlocks between the nanofibers and the coating matrix can form to improve the mechanical properties of the coating systems containing nanofibers^{17,18}. Also, the diameter of these fibers is usually on the submicron scale. Therefore, it is possible to incorporate these fibers within relatively thin coatings, e.g., those with a thickness of only several micrometers^{15,19}. Most importantly, nanofibers are continuous and intertwined, so the embedded inhibitors can readily transport through the interconnected channels to a damaged area, replenishing released inhibitors to provide long-term healing performance^{13,20}. As proven in a previous study²¹, nanofibers can repetitively suppress the recurrence of corrosion, whereas a single healing event was observed when microspheres were used. It should be noted that the release of healing agents from the nanofibers in that work was induced by an external mechanical force. However, other stimuli, such as water penetration and local pH changes, may also be generated during the corrosion process and can be used as triggers for releasing protective species. Among these stimuli, local pH alteration is preferable as spatially separated anodic and cathodic reactions occurring during corrosion of aluminum alloys drive the local environments to become acidic and basic, respectively^{22,23}. Accordingly, pH-sensitive nanofibers can release entrapped corrosion inhibitors as the pH changes, while reserving the inhibitors once corrosion is retarded and the pH is restored to neutral or near neutral. Nevertheless, to the best of our knowledge, the majority of nanofibers developed to date are either not stimulus-responsive or only sensitive to water penetration^{12,14,15,24}. A few earlier works attempted to develop inhibitor-loaded nanofibers using the change of pH as the release trigger, but most nanofibers could only respond to either acidic or alkaline pH conditions^{25,26}. Although a previous study reported that the nano-scale fibers made from polyaniline could be dual-pH sensitive²⁷, those fibers did not have continuous length and the nanofiber network was not observed. This may lead to difficulty in

¹Fontana Corrosion Center, Department of Materials Science and Engineering, The Ohio State University, Columbus, OH 43210, USA. ✉email: frankel.10@osu.edu

transporting the impregnated inhibitors to achieve repeated self-healing performance. Hence, it is worthwhile to put more effort into fabricating inhibitor-loaded nanofibers that are responsive to both low and high pH conditions and capable of constantly releasing the entrapped inhibitors in the same defective regions.

To engineer nanofibers containing corrosion inhibitors, the electrospinning technique is one of the most promising methods due to its flexibility and easy operation. This one-step technique can produce long and continuous fibers with a diameter of nanometers or larger. The physical properties such as the morphology, porosity, and diameters of the fibers can be readily modified by tuning the electrospinning parameters, providing a possibility of manufacturing a variety of nanofibers with desired properties^{18,24}. However, the electrospinning technique is not widely explored in the context of corrosion, especially for the fabrication of dual-pH-sensitive nanofibers for corrosion protection applications. Therefore, the aim of this study is to use the coaxial electrospinning technique to encapsulate corrosion inhibitors into nanofibers with the chitosan/PAA polyelectrolyte coacervate as the shell material. As described in a previous work²⁸, the chitosan/PAA polyelectrolyte coacervate could be electrospun to form nanofibers. Although the swelling/deswelling behavior of as-spun nanofibers was only reported at the neutral and acidic pH conditions, these nanofibers might also respond to the pH shift towards alkaline regions. This is because both chitosan and PAA are weak polyelectrolytes and the charge density on their polymer chains is dependent on the pH of the surrounding medium, so the interactions between the polyelectrolytes can potentially be affected by both acidic and alkaline pH^{29–31}. This assumption has also been validated in prior works where materials made from weak/weak polyelectrolyte pairs were damaged at both low and high pH conditions but remained stable at neutral pH^{32,33}. Therefore, the chitosan/PAA polyelectrolyte coacervate can be an excellent candidate for the shell material of dual-pH-responsive nanofibers. To assess the applicability of generating corrosion inhibiting nanofibers, $\text{Ce}(\text{NO}_3)_3$ was loaded in the cores of the fibers via the coaxial electrospinning technique. $\text{Ce}(\text{NO}_3)_3$ is considered as a mixed inhibitor because Ce^{3+} ions are highly

efficient in retarding cathodic reactions of aluminum alloys, whereas NO_3^- ions inhibit anodic kinetics to some extent^{34–36}. Furthermore, it raises less concerns about toxicity issues than hexavalent-chromium-based inhibitors^{37,38}. Thus, $\text{Ce}(\text{NO}_3)_3$ -loaded nanofibers were created by electrospinning, and their core-shell structure, morphology, and composition were characterized by confocal spectroscopy, transmission electron microscopy (TEM), and scanning electron microscopy (SEM) with energy dispersive spectroscopy (EDS). The release behavior of the nanofibers in response to pH alterations was monitored by UV-vis spectroscopy. Afterwards, a pH-sensitive coating was developed by embedding $\text{Ce}(\text{NO}_3)_3$ -loaded nanofibers into a polyvinyl butyral (PVB) coating matrix and applied on a AA2024-T3 substrate. The corrosion resistance of the coated sample was studied comprehensively by electrochemical impedance spectroscopy (EIS). Furthermore, EIS was also conducted on a scratched coating sample to determine the self-healing capability over time.

RESULTS AND DISCUSSION

Dual-pH-sensitive behavior of chitosan/PAA polyelectrolyte coacervate

A previous study described how chitosan and PAA could form a homogenous coacervate solution without precipitates in an acidic environment²⁸, but the dual-pH-sensitive behavior of the coacervate was not studied. Therefore, to have a quick demonstration of the dual-pH-sensitivity of the coacervate, bromophenol blue (BB), an organic dye-loaded coating, i.e., $(\text{BB})_3/(\text{chitosan/PAA})_5$ was fabricated and the release of the entrapped BB at different pH conditions was studied. BB was impregnated into the polyelectrolyte coacervate coating because the released BB can be easily detected by the color change of the release medium without need of further characterization techniques. As shown in Fig. 1a, the media after 24 h of release appears to be yellow in color at both pH 2.5 and 10, whereas a less significant change is observed at pH 7. This proves the chitosan/PAA coacervate is dual-pH-responsive and can release BB at both low and high pH conditions at a faster rate than that at neutral pH. Another set of coating samples

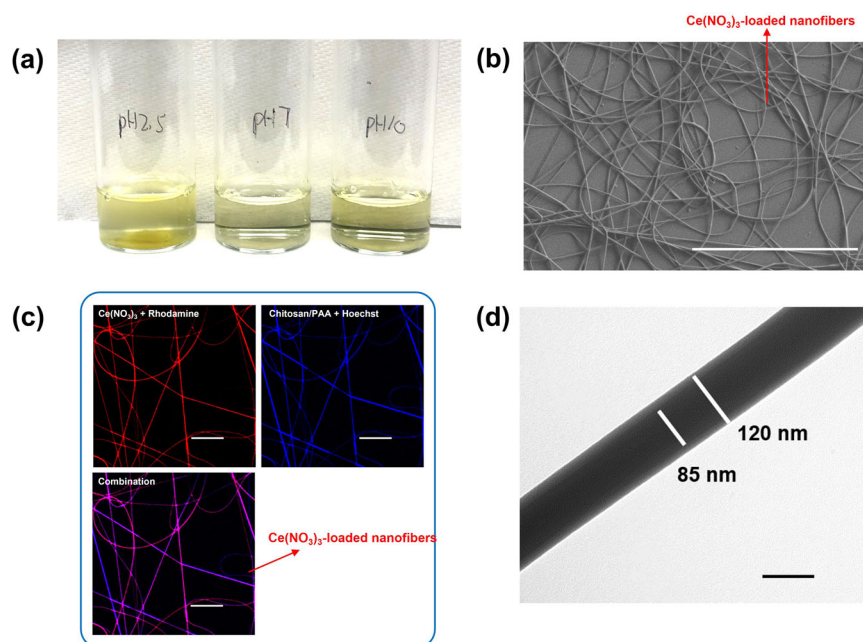


Fig. 1 Dual-pH-responsive behavior of the chitosan/PAA coacervate and characterization of $\text{Ce}(\text{NO}_3)_3$ -loaded nanofibers. **a** The release of BB in DI water with varied pH for 24 h. **b** The surface morphology of $\text{Ce}(\text{NO}_3)_3$ -loaded nanofibers examined by SEM. Scale bar is 20 μm . **c** $\text{Ce}(\text{NO}_3)_3$ -loaded nanofibers observed by confocal spectroscopy. Scale bar is 20 μm . **d** The core-shell structure of an individual $\text{Ce}(\text{NO}_3)_3$ -loaded nanofiber confirmed by TEM. Scale bar is 100 nm.

without BB was used to detect the alteration of surface morphology caused by immersion for 24 h. From optical microscopy images (Supplementary Fig. 1), most of the coating dissolved at pH 2.5, and several large pores were created at pH 10. At pH 7, the surface morphology became rougher relative to that before immersion, but this change is less obvious compared to that at pH 2.5 and 10. This finding again verifies that the chitosan/PAA coacervate is sensitive to both the acidic and basic pH conditions. The mechanism behind this pH-responsive behavior is associated with the strength of electrostatic interactions between the two oppositely charged polyelectrolytes^{28,39}. As well-documented in earlier works, the pK_a values of chitosan are 6.22, 6.11, and 6.09, whereas PAA has a pK_a of 6.5^{29,40}. Although these pK_a values may shift when the polyelectrolyte is incorporated within the coacervate⁴¹, it is safe to conclude that chitosan and PAA have moderate interactions between their functional groups at pH 7 as both polyelectrolytes are partially charged. However, such interactions can be compromised by altering the pH to 2.5 or 10, owing to the deionization of PAA or chitosan, respectively. As a result, the presence of hydrogen bonds between water and uncharged functional groups within polyelectrolytes (i.e., carboxylic acid groups in PAA and amine groups in chitosan) enables water to penetrate through the polymer networks, a process accompanied by the swelling/dissolution of the polyelectrolyte coacervate²⁸. Moreover, in both the acidic and alkaline environments, one of the polyelectrolytes is prone to be fully charged and the stronger repulsive force within the polyelectrolytes can also cause the polyelectrolyte coacervate to swell or dissolve in the solution. Consequently, the impregnated organic dye can rapidly release from the unstable polyelectrolyte coacervate at pH 2.5 and 10.

Characterization of $Ce(NO_3)_3$ -loaded nanofibers

$Ce(NO_3)_3$ -loaded nanofibers were fabricated by the electrospinning technique. A coaxial nozzle was utilized to prevent the undesired mixing between the polyelectrolyte coacervate solution and the inhibitor solution prior to the formation of nanofibers. During the electrospinning process, chitosan may have limited electrospinnability due to the intermolecular interactions^{42,43}, but the presence of PAA in the polyelectrolyte coacervate can hinder the undesired interactions between the chitosan chains allowing electrospinning to be successful⁴⁴. The SEM in Fig. 1b shows that the resulting nanofibers are free of defects and beads. The diameter of the electrospun nanofibers is less than 200 nm (Supplementary Fig. 2).

To verify the core-shell structure of the nanofibers, confocal spectroscopy was employed at first. Hoechst 33258 pentahydrate was added into the shell solution while rhodamine B was mixed with the core solution. Due to the excitation by the laser in the confocal microscope, these two fluorescence dyes made the shell and the core blue and red in color, respectively. However, due to the limited resolution of confocal microscopy, the shell of the nanofibers appears to be solid instead of hollow (Fig. 1c). The image of the core stained by rhodamine B base is continuous, indicating $Ce(NO_3)_3$ is filled within the nanofibers. Upon combining the images of the shell and the core, the red and blue colors overlap, and no red color is observed outside the nanofibers, suggesting the successful incorporation of $Ce(NO_3)_3$ (Fig. 1c). To further confirm $Ce(NO_3)_3$ was incorporated within the nanofibers, EDS was carried out by analyzing the Ce spectral $M\alpha$ line located at 0.88 keV⁴⁵. No other spectral lines of Ce at high energy levels were examined to prevent the signal of Ce from being overwhelmed by background signals from the substrate. Besides, the $M\alpha$ line of Ce did not overlap with spectral lines of other elements contained in the samples, such as O, C, and N. Therefore, it is feasible to only use the $M\alpha$ line to investigate the existence of Ce inside the nanofibers. Three locations along one nanofiber were

randomly selected and examined. The content of Ce was independent of location (Supplementary Fig. 3a), indicating the uniform dispersion of $Ce(NO_3)_3$ in the nanofibers. Additionally, the possible existence of Ce in an area without nanofibers was probed, but the characteristic peak of Ce did not appear in the EDS spectrum (Supplementary Fig. 3b). This validates the successful encapsulation of $Ce(NO_3)_3$, consistent with the confocal spectroscopy result (Fig. 1c). Since the confocal spectroscopy was not able to reveal the core-shell structure of the nanofibers, TEM analysis was conducted. The detailed morphology of the nanofibers is presented in Fig. 1d. A sharp boundary between relatively dark and bright regions is identified, corresponding to the core and shell of the nanofibers, respectively. This is in line with previous studies showing that the element with a higher atomic number is more likely to scatter electrons relative to that with a low atomic number, rendering a darker region in the resulted bright-field TEM image^{46,47}. Therefore, the core enriched with $Ce(NO_3)_3$ was darker compared to the shell made from the polyelectrolyte coacervate. The overall diameter of the nanofiber is about 120 nm, while the diameter of the core region is around 85 nm. Moreover, the core is concentrically located in the nanofibers, suggesting a stable electrospinning process^{48,49}. The use of the coaxial electrospinning technique minimizes the contact between the core and shell solutions⁵⁰, avoiding the adverse effect of the electrostatic interaction between $Ce(NO_3)_3$ and the polyelectrolyte coacervate and contributing to the successful fabrication of $Ce(NO_3)_3$ -loaded nanofibers.

Release of Ce(III) from $Ce(NO_3)_3$ -loaded nanofibers

The dual-pH-responsive behavior of the chitosan/PAA polyelectrolyte coacervate was corroborated by the fast release of an organic dye upon a pH change (Fig. 1a and Supplementary Fig. 1). However, it is essential to investigate whether this behavior can be affected by the electrospinning process. Moreover, the presence of $Ce(NO_3)_3$ in the core of the nanofibers may also result in different release kinetics due to the undesired electrostatic attraction between the negatively charged PAA and positively charged cerium ions. Therefore, the release of $Ce(NO_3)_3$ from the nanofibers was studied by immersing the nanofiber-coated samples in DI water with pH 2.5, 7, or 10. The exposed area was 7.5 cm². It should be noted that although both cerium ions and nitrate ions can be released from the nanofibers, it is difficult to detect the released nitrate ions by UV-vis spectroscopy. Thus, only the released amounts of Ce(III) were measured, and the cumulative release profile of Ce(III) is shown in Fig. 2a. There are two stages in the release curves including a rapid release of Ce(III) at the beginning and a sustained release thereafter. The initial burst release of Ce(III) may be associated with unleashing the inhibitors close to the shell, which is commonly reported in the literature^{32,51}. As time proceeds, the corrosion inhibitors in the inner core are released, contributing to the sustained release at a slower rate in the second stage. Notably, the release rate in the first stage was higher at pH 2.5 and 10, as indicated by the steeper slope of the release curve, compared to that at pH 7. This can be elaborated by the pH-triggering release process at both low and high pH conditions. After 2 h of exposure, the final values of the cumulative concentration of Ce(III) were 0.16 mM at pH 2.5 and 0.14 mM at pH 10. The enhanced solubility of Ce(III) at low pH conditions may account for a faster release of Ce(III) at pH 2.5 compared to at pH 10^{34,52}. Although Ce(III) ions tend to precipitate at pH 10, which is thermodynamically favorable, it is likely a kinetically slow process. It should be noted that the released amounts of Ce(III) at both acidic and alkaline pH were more than twice that at the neutral pH, verifying that the $Ce(NO_3)_3$ -loaded nanofibers are dual-pH-sensitive, and neither the electrospinning process nor the enclosed $Ce(NO_3)_3$ substantially interfere with the pH-sensitive release behavior of the nanofibers. Moreover, the

release profile of Ce(III) displayed curves with a positive slope at the end of the release study, especially at both low and high pH conditions, indicating the enclosed $\text{Ce}(\text{NO}_3)_3$ was not depleted and was capable of sustainably releasing for extended periods. This enduring release process may have provided a sufficient amount of corrosion inhibitors for corrosion protection of AA2024-T3. It is possible that higher contents of $\text{Ce}(\text{NO}_3)_3$ in the fibers could be achieved by adjusting the electrospinning parameters, but this was not investigated. The surface morphology of the nanofibers after the release study was also examined by SEM. As shown in Fig. 2b, the nanofibers strongly dissolve after being exposed to an acidic condition for 2 h. In an alkaline environment, a large number of nanofibers swell, and numerous pores are generated inside the nanofiber networks (Fig. 2b and

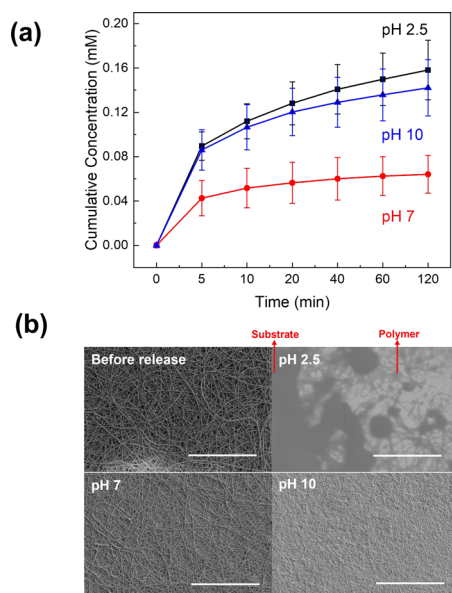


Fig. 2 Release by $\text{Ce}(\text{NO}_3)_3$ -loaded nanofibers at different pH conditions. **a** Cumulative release profiles of $\text{Ce}(\text{NO}_3)_3$ -loaded nanofibers in DI water with varied pH. **b** The surface morphology of $\text{Ce}(\text{NO}_3)_3$ -loaded nanofibers before and after the release study. The release study was performed for 2 h. Scale bar is 50 μm .

Supplementary Fig. 4). In contrast, the change in the surface morphology of the nanofibers at pH 7 is negligible (Fig. 2b). It is also worth noting that the nanofibers seem to exhibit a higher degree of swelling under acidic condition compared to that of the alkaline condition, which may explain the higher amount of Ce(III) released at pH 2.5 than pH 10 (Fig. 2a). The distinct morphologies of the nanofibers shown in Fig. 2b suggest that the shell material can be in an either open or close state depending on the environmental pH. Under acidic and alkaline conditions, the shell of the nanofibers can open to release the encapsulated corrosion inhibitors, whereas remains closed at neutral pH to retard the leakage of the inhibitors from the core of the nanofibers.

Surface morphology of coated AA2024-T3 samples

Two coated AA2024-T3 samples, i.e., Fiber-PVB and Ce-Fiber-PVB were prepared using the dip-coating method. The coating made by the bar-coating technique might have unfilled interfibrillar pores/voids inside the coating, which can serve as pathways for the aggressive solution to reach the AA2024-T3 substrate to trigger corrosion. Additionally, the electrospun nanofibers formed a mat that was thick enough to be readily peeled off from the substrate during the bar-coating process, even though PVB was precoated on AA2024-T3 to enhance the adhesion between the nanofiber mat and the metal substrate. As a result, visible defects were inevitably created in the resulting coated samples (Supplementary Fig. 5a). As the nanofiber mat was found to not dissolve in ethanol, a dip-coating method was used as an alternative to prepare coated AA2024-T3 samples. The surface morphology of dip-coated samples was explored by SEM. Compared to PVB (Fig. 3a), the inclusion of nanofibers with/without $\text{Ce}(\text{NO}_3)_3$ did not significantly alter the surface morphology, and the nanofibers seemed to be fully covered by PVB (Fig. 3b, c). Moreover, the thickness of Fiber-PVB and Ce-Fiber-PVB was 17 and 16 μm , respectively, which did not evidently increase compared to that of PVB. This is possibly because PVB intercalated into the nanofiber mat and reached the underlying metal substrate. Hence, by dip-coating, PVB can seal the interfibrillar pores and act as a binder for the nanofiber mat to attach to the metal substrate. During the coating preparation, the nanofiber mat formed on the substrate was white in color but gradually became transparent with the deposition of PVB layers, indicating the infiltration of PVB to replace the air in the interfibrillar pores, in line with studies

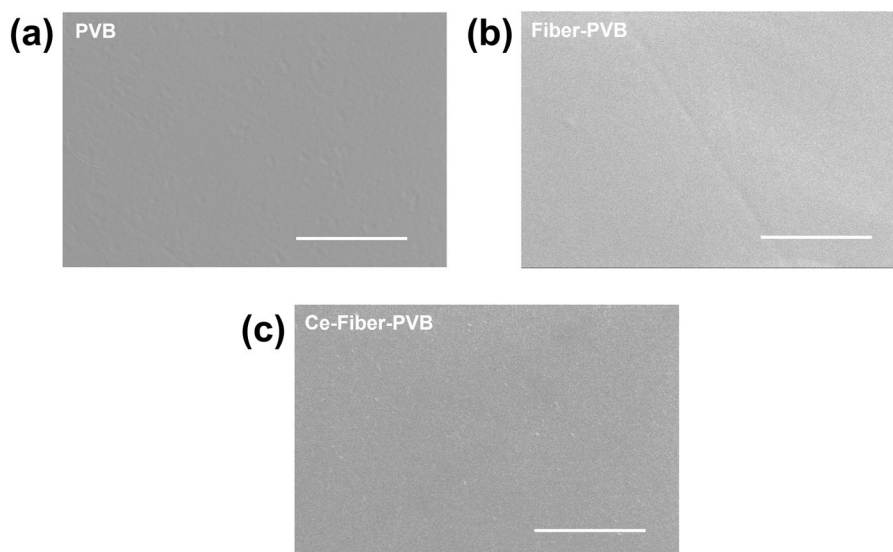


Fig. 3 Characterization of coating samples by SEM. Surface morphologies of AA2024-T3 dip-coated with **a** PVB, **b** Fiber-PVB, **c** Ce-Fiber-PVB examined by SEM. Scale bar is 50 μm . The thicknesses of PVB, Fiber-PVB, and Ce-Fiber-PVB were 14, 17, and 16 μm , respectively.

reported elsewhere^{15,53}. Unlike the bar-coated samples, the dip-coated samples had a smooth and uniform surface without noticeable defects (Supplementary Fig. 5a). The advantage of the dip-coating method over the bar-coating technique was further demonstrated by the surface morphology of coated samples observed by SEM. As shown in Supplementary Fig. 5b, nanofibers partially protrude from the bar-coated samples, which is not the case for the dip-coated samples (Fig. 3). These uncovered parts of nanofibers may jeopardize the integrity of the coating and be vulnerable sites for corrosion attack. Therefore, the dip-coating method was utilized to fabricate coated AA2024-T3 samples for the following electrochemical tests.

EIS tests at various pH conditions

EIS measurements were carried out at both pH 2.5 and pH 10 to examine the corresponding corrosion resistance of two coated samples, i.e. Fiber-PVB and Ce-Fiber-PVB, both on AA2024-T3, as a function of immersion time. The solution pH was adjusted to be acidic and basic to mimic the situation that occurred in anodic and cathodic sites in the metal substrate during corrosion, because the local pH conditions may decrease or increase due to the hydrolysis of metal ions and the oxygen reduction reaction (ORR), respectively^{54,55}. As a comparison, EIS tests at pH 7 were also conducted. The addition of 5 mM Na₂SO₄ ensures enough conductivity of the electrolyte. Meanwhile, such a small amount of Na₂SO₄ is not likely to adversely affect the stability of the nanofibers or trigger corrosion of AA2024-T3. For reproducibility, the EIS tests were repeated twice. The representative EIS spectra are shown in Fig. 4, and the impedance values at 0.01 Hz ($|Z|_{0.01\text{Hz}}$) for different immersion times is recorded in Supplementary Fig. S6 to better illustrate the corrosion protection performance of coated samples, as a higher value of low-frequency impedance generally indicates better corrosion resistance⁵⁶.

For Fiber-PVB immersed at pH 2.5 (Fig. 4a and Supplementary Fig. 6a), the impedance values at both low and middle frequency abruptly decreased by over one order of magnitude after the coating was soaked in the solution for 24 h. This indicates that the coating began to degrade, and water was absorbed by the coating at a rapid rate. Then, a slight decrease in the impedance values was observed as the immersion time increased from 24 to 48 h, which is possibly associated with the water saturation in the coating. With a prolonged soaking time, the impedance value at low frequency further showed a downward trend, perhaps because the corrosive electrolyte arrived at the metal substrate to initiate corrosion. Meanwhile, the nanofibers inside the coating were destroyed, which accelerated the rupture of the coating. In the Bode phase plots, two time constants are clearly present with one at high frequency and the other at low frequency, related to the coating property and the charge transfer process at the metal/coating interface, respectively^{57,58}. The maximum phase angle at the high frequency was low and the magnitude decreased over time. No plateau in the high frequency range in the Bode phase plot is observed. These results suggest that the barrier property of the coating sample was severely affected by exposure to an aggressive environment. In contrast, at pH 2.5 the impedance values for Ce-Fiber-PVB with Ce(NO₃)₃ encapsulated within the nanofibers displayed a constant increase at low frequencies along with a moderate increase in the mid frequency range (Fig. 4b and Supplementary Fig. 6a). Additionally, the phase angle at high frequencies is nearly -90° and seems to be constant at all immersion times. Besides, the plateau region in the high frequency range tends to broaden towards the lower frequency, indicating the barrier property of the coating is promoted rather than being undermined. All these observations suggest Ce-Fiber-PVB has better corrosion resistance than Fiber-PVB, possibly originated from the corrosion inhibition effect of Ce(NO₃)₃. As

previously reported, Ce(NO₃)₃ is highly efficient in retarding corrosion of AA2024-T3 through the preferential deposition at cathodic sites to form insoluble cerium oxide/hydroxide films^{59,60}. Moreover, the charge transfer process between the anodes and cathodes can also be impeded due to the lower conductivity of precipitated cerium compounds, thus reducing the corrosion rate of AA2024-T3^{61,62}. Some works also suggested that Ce(IV) species can be generated by the oxidation of Ce(III) during the corrosion of AA2024-T3, and these species can also form insoluble Ce(IV) oxides/hydroxides to slow down the corrosion process^{63,64}. In contrast to cerium ions, which are cathodic inhibitors, nitrate ions can impede anodic reactions to some extent at low pH conditions. This is possibly due to the oxidizing capability of nitrate ions, which can promote the formation of a protective oxide layer to passivate the metal surface³⁴. As shown in Supplementary Fig. 7, the anodic current density of AA2024-T3 decreased when the metal was polarized in the acidic solutions containing Ce(NO₃)₃, which may be associated with the existence of nitrate ions. Therefore, for Ce-Fiber-PVB, Ce(NO₃)₃ was released from the nanofibers and can potentially retard both anodic and cathodic kinetics, leading to the improved corrosion protection performance. However, the formation of an insoluble cerium film can be delayed by the limited local pH raise under an acidic bulk environment, and a stable film is more difficult to be maintained at low pH conditions, leading to a modest drop in $|Z|_{0.01\text{Hz}}$ after 72 h immersion (Supplementary Fig. 6a).

The behavior at pH 10 was similar. For Fiber-PVB (Fig. 4c and Supplementary Fig. 6b), after 1 h of immersion, the impedance modulus declined with decreasing frequency due to the drastic alteration of the metal surface caused by corrosion. The addition of the empty nanofibers did not provide corrosion protection to the metal substrate, evidenced by a continuous drop in $|Z|_{0.01\text{Hz}}$ (Supplementary Fig. 6b). The impedance at the middle frequency decreased with increasing immersion time, and the plateau at the middle frequency was more distinctly shown in the extended immersion periods, indicating the degradation of the coating and the ingress of corrosive electrolyte (Fig. 4c). On the other hand, $|Z|_{0.01\text{Hz}}$ of Ce-Fiber-PVB increased over time and was nearly two orders of magnitude higher than that of Fiber-PVB by the end of immersion, suggesting superior corrosion resistance (Supplementary Fig. 6b). It should be noted that in the Bode phase plot (Fig. 4d), the time constant at high frequency is dominant. Although a small bump appears at low frequency after 1 h of immersion, it diminishes with immersion time. This implies the released Ce(NO₃)₃ slowly suppresses corrosion of AA2024-T3. This inhibition effect is better than that at pH 2.5, as indicated by no decrease in $|Z|_{0.01\text{Hz}}$ of Ce-Fiber-PVB after 72 h of immersion. This is likely account of the easier formation of insoluble cerium oxides/hydroxides in the alkaline environment^{56,65}.

At pH 7 the behavior was different. For Fiber-PVB (Fig. 4e), the impedance values at both low frequency and middle frequency declined by an approximately full decade. However, they did not keep decreasing after 24 h, and $|Z|_{0.01\text{Hz}}$ even recovered to some extent in the repeated EIS experiment (Supplementary Fig. 6c), which is not the case at pH 2.5 and pH 10. It is well-known that both PAA and chitosan are hydrophilic and chitosan has multiple sites on the polymer chains for water adsorption, such as hydroxyl groups and amine groups^{40,66}. The introduction of the nanofibers into the coating may render the coating system to be hydrophilic, which can speed up the water infiltration. As a result, a decrease in the impedance values was shown even though the coating was not severely deteriorated. Since the environment is less aggressive at pH 7, the corrosion rate of AA2024-T3 is low, which can explain why the impedance remained unchanged with extended immersion time. For Ce-Fiber-PVB (Fig. 4f and Supplementary Fig. 6c), the released Ce(NO₃)₃ may have precipitated to form an insoluble film to retard water penetration, so the impedance values of Ce-Fiber-PVB did not decrease. Nevertheless, since the chitosan/PAA

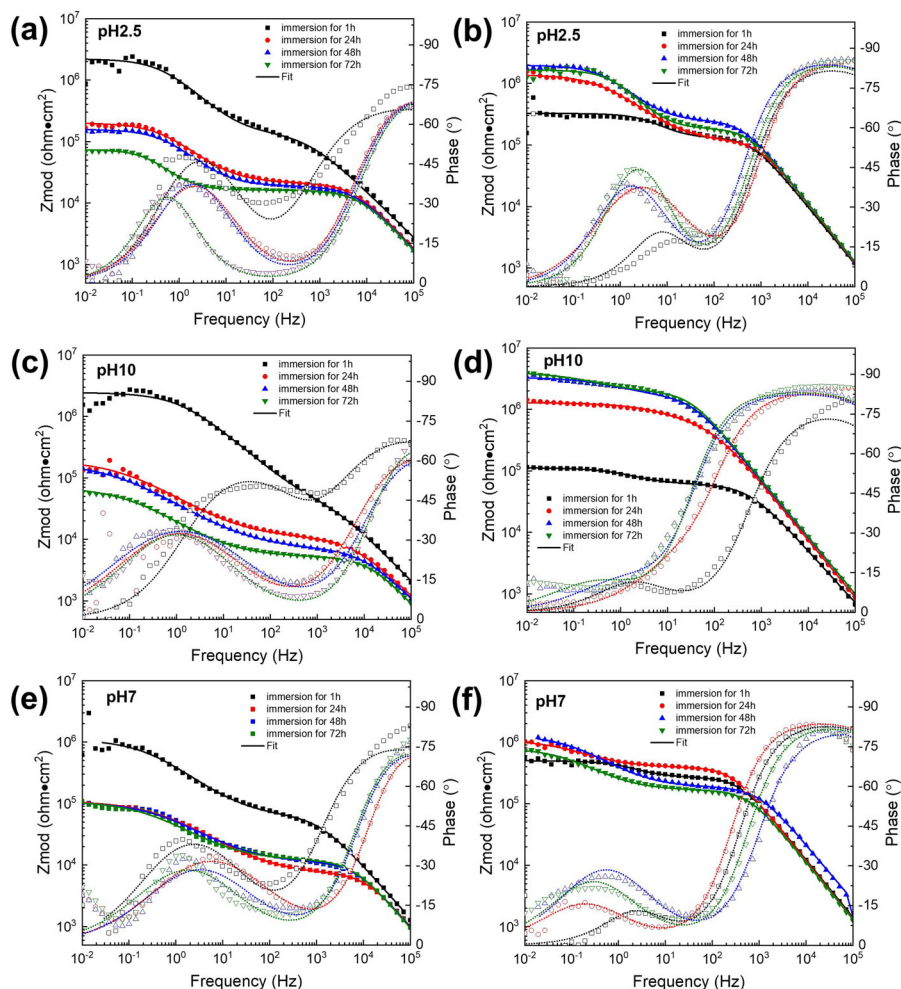


Fig. 4 EIS measurements at different pH conditions. Different coated samples corroded in 5 mM Na_2SO_4 with varied pH conditions: **a** Fiber-PVB at pH 2.5; **b** Ce-Fiber-PVB at pH 2.5; **c** Fiber-PVB at pH 10; **d** Ce-Fiber-PVB at pH 10; **e** Fiber-PVB at pH 7; and **f** Ce-Fiber-PVB at pH 7.

coacervate is stable at pH 7, a limited amount of entrapped Ce (NO_3)₃ can be released out from the nanofibers. Thus, unlike at pH 2.5 and 10, the impedance did not significantly increase with increasing immersion time at pH 7.

To quantitatively estimate the protectiveness of the coating in Na_2SO_4 solutions with various pH, EIS experimental data were fitted using a classical equivalent circuit model with two time constants, presented in Supplementary Fig. 8a, and the fitted lines are exhibited along with the experimental data in Fig. 4. The selection of this model considers the following characteristics: R_s is the solution resistance. R_{pore} and CPE_{coat} correspond to the pore resistance and the coating capacitance indicated by a constant phase element, respectively. R_p refers to the polarization resistance whereas CPE_{dl} represents the double layer capacitance, arising from the faradic process at the coating/metal interface. Due to the heterogeneity and roughness of the coating surface²⁵, the maximum phase angle deviated from -90° (Fig. 4). As a result, constant phase elements (CPEs) were applied instead of perfect capacitors for a more accurate fit, which can take into account the non-ideal capacitive behavior of coated samples. To demonstrate differences in the corrosion resistance of Fiber-PVB and Ce-Fiber-PVB, the evolution of R_{pore} and R_p versus immersion time are compared and shown in Figs. 5 and 6, while the actual coating capacitance (C_{coat}) and double layer capacitance (C_{dl}) were extracted from the fitting results using a well-established method⁶⁷, and provided in Supplementary Figs. 9 and 10.

Generally speaking, R_{pore} represents the barrier property of a coating system, and a larger R_{pore} reflects stronger protective capability of the coating. As displayed in Fig. 5a, R_{pore} decreased by nearly a full decade within 24 h of immersion when Fiber-PVB was placed in Na_2SO_4 solution with pH 2.5 because of rapid water saturation in the coating. This is also consistent with a sudden increase in C_{coat} at the initial stage of immersion (Supplementary Fig. 9a). Afterwards, R_{pore} continued diminishing from 2.0×10^4 ohm cm^2 to 1.6×10^4 ohm cm^2 , possibly due to the destabilization of the embedded nanofibers. As mentioned above, under acidic pH conditions, the electrostatic interactions between chitosan and PAA are more likely to be disrupted, inducing the swelling/dissolution of the nanofibers. Therefore, more defects can form in the coating to adversely affect the protection properties of the coating system. Due to the same reason, a similar declining tendency in R_{pore} of Fiber-PVB with immersion time was observed at pH 10 (Fig. 5b). Concerning pH 7 (Fig. 5c), the average R_{pore} value of Fiber-PVB also declined from 5.5×10^4 ohm cm^2 to 7.9×10^3 ohm cm^2 during the early immersion period, but then slightly recovered to around 1.0×10^4 ohm cm^2 for the remaining exposure time. At the end of the EIS measurement, the decrease in R_{pore} was less significant compared to that displayed at pH 2.5 and 10. This is because the coating has a slower degradation rate and nanofibers are primarily intact under a less corrosive environment. It should be noted that despite the mild environment (i.e., pH 7), an abrupt decrease in R_{pore} during the first 24 h immersion was again observed. This is possibly due to the fast

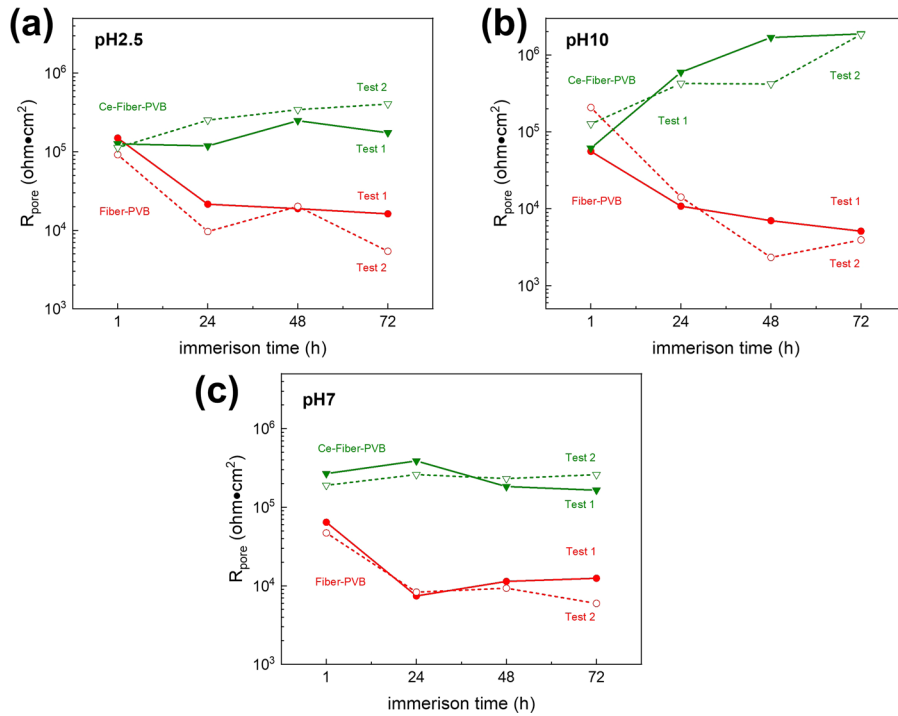


Fig. 5 Evolution of R_{pore} of Fiber-PVB and Ce-Fiber-PVB at different pH conditions. Coated samples were immersed in 5 mM Na_2SO_4 with pH **a** 2.5, **b** 10, **c** 7.

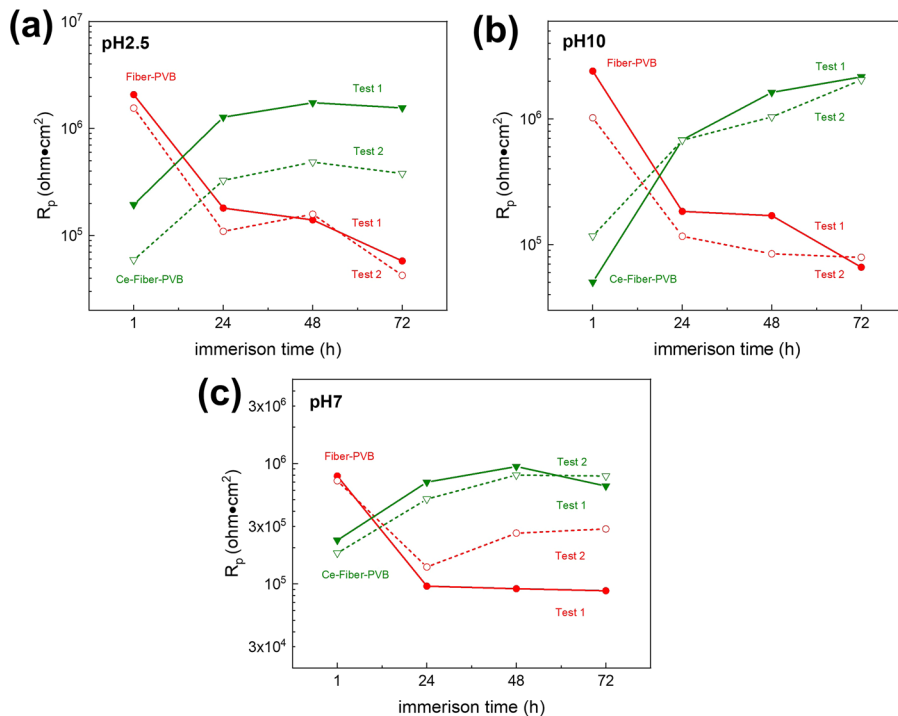


Fig. 6 Evolution of R_p of Fiber-PVB and Ce-Fiber-PVB at different pH conditions. Coated samples were immersed in 5 mM Na_2SO_4 with pH **a** 2.5, **b** 10, **c** 7.

water infusion into the coating with an intrinsic hydrophilic property, which can be a factor of concern and needs to be addressed in future work. For Ce-Fiber-PVB in pH 2.5, R_{pore} either barely changed or had a modest rise in the replicated EIS tests (Fig. 5a). This is significantly different from what was observed for Fiber-PVB at the same pH condition. The higher corrosion resistance of Ce-Fiber-PVB may be attributed to the additional

protection from the released cerium species and the subsequent formation of insoluble cerium films. Nevertheless, these insoluble films are prone to be redissolved upon contacting with the acidic electrolyte, resulting in a limited improvement in the barrier property of the coating. However, at alkaline pH condition redissolution of the oxide/hydroxide does not occur. At pH 10, R_{pore} exhibited a value of 2.0×10^6 $\text{ohm}\cdot\text{cm}^2$ at the end of the EIS

measurement, which was over one order of magnitude higher than the initial value (Fig. 5b). Meanwhile, C_{coat} decreased over time (Supplementary Fig. 9b). These results suggest a greatly enhanced protective ability of the coating due to the favorable pH condition for the formation of a robust cerium hydroxide/oxide film. At pH 7 (Fig. 5c), R_{pore} stayed unchanged throughout the exposure, which is similar to what was observed at pH 2.5, but the mechanism is different. At neutral pH, a fast release of loaded $\text{Ce}(\text{NO}_3)_3$ is hampered by the undamaged shell of the nanofibers, so the protective ability of the coating cannot be dramatically boosted due to the inadequate released corrosion inhibitors. Nevertheless, a small amount of corrosion inhibitors can still be released by diffusion and provide protection to some degree. As a result, no decrease in R_{pore} was shown.

It is noteworthy that for the two coating samples under study, the variation of R_{pore} versus immersion time was not obvious, possibly because water quickly saturated inside the coating. Therefore, the evolution of R_p over time was also assessed to characterize corrosion protection performance of the coated samples, as R_p is inversely correlated with the rate of corrosion and can describe the corrosion resistance of the coated samples in an aggressive environment. For Fiber-PVB corroded at pH 2.5, R_p decreased over time while C_{dl} increased (Fig. 6a and Supplementary Fig. 10a). For instance, R_p diminished from $2.1 \times 10^6 \text{ ohm cm}^2$ to $1.8 \times 10^5 \text{ ohm cm}^2$ when the coating was immersed in the solution for 24 h, then continuously decreased at a slower rate for the remaining immersion period. In the meantime, C_{dl} notably increased from $1.0 \times 10^{-8} \text{ F cm}^{-2}$ to $3.0 \times 10^{-6} \text{ F cm}^{-2}$ throughout the immersion. These results indicate coating degradation and the fast ingress of the aggressive electrolyte towards the metal surface to trigger corrosion. A similar trend was also found for R_p and C_{dl} of Fiber-PVB at pH 10 (Fig. 6b and Supplementary Fig. 10b). Like pH 2.5, the coating sample experienced a severe deterioration due to the swelling of the nanofibers. As a result, more pathways were generated for the aggressive electrolyte to arrive at the AA2024-T3 substrate, causing a sudden change in R_p and C_{dl} within a short immersion period. Due to the amphoteric nature of Al, AA2024-T3 is also highly vulnerable to corrosion at alkaline conditions, leading to the decrease and increase of R_p and C_{dl} , respectively. However, at pH 7, despite a drop in R_p during the first 24 h immersion, Fiber-PVB seemed to have constant R_p values up to 72 h (Fig. 6c), which is associated with the higher stability of the passive film on the substrate at neutral pH. Even though water diffuses to the metal/coating interface and leads to the reduction of R_p at the beginning of immersion, intense corrosion of AA2024-T3 was impeded by the passive film, resulting in the unchanged R_p of Fiber-PVB between 24 and 72 h. For Ce-Fiber-PVB corroded at pH 2.5, R_p increased and reached a plateau above $1.0 \times 10^6 \text{ ohm cm}^2$ until the exposure time extended to 48 h, then slightly reduced between 48 and 72 h (Fig. 6a). Nevertheless, compared to that of Fiber-PVB, the final R_p of Ce-Fiber-PVB was more than one order of magnitude higher, suggesting a lower corrosion activity when AA2024-T3 was coated with Ce-Fiber-PVB. The detailed mechanism has been discussed above. To recap, the encapsulated $\text{Ce}(\text{NO}_3)_3$ was stored within the nanofibers, and released when the nanofibers were open at pH 2.5, followed by precipitating insoluble cerium oxides/hydroxides to passivate the metal surface. Since this insoluble film has a lower dielectric constant, C_{dl} of Ce-Fiber-PVB decreased and became lower than that of Fiber-PVB (Supplementary Fig. 10a). It should be noted that under the acidic pH condition, the local pH raise is buffered by the bulk acidic solution, so the formation of the cerium oxide/hydroxide film is restrained. This may lead to partial coverage of the film on the metal surface, limiting the corrosion inhibition effect of released $\text{Ce}(\text{NO}_3)_3$. Similarly, at pH 10, the addition of $\text{Ce}(\text{NO}_3)_3$ -loaded nanofibers empowered the coating sample with greater corrosion protection. R_p climbed from $5.0 \times 10^4 \text{ ohm cm}^2$ to $2.1 \times 10^6 \text{ ohm cm}^2$, whereas C_{dl} markedly decreased over time (Fig. 6b and

Supplementary Fig. 10b). The alkaline pH condition facilitates the generation of a more robust cerium film on the AA2024-T3 surface, so R_p did not suffer a decrease with longer immersion. Considering pH 7, the nanofiber was in a closed state owing to the moderate electrostatic interactions between the chitosan and PAA, so a low amount of $\text{Ce}(\text{NO}_3)_3$ could be released, resulting in less visible changes in R_p and C_{dl} (Fig. 6c and Supplementary Fig. 10c). In general, incorporating $\text{Ce}(\text{NO}_3)_3$ -loaded nanofibers into the PVB coating matrix can improve the corrosion inhibition efficacy, while enclosing empty polyelectrolyte coacervate nanofibers does not significantly increase the corrosion resistance of AA2024-T3.

EIS measurements in NaCl solutions

To further evaluate the resistance of Fiber-PVB and Ce-Fiber-PVB against corrosion, EIS spectra were also recorded in 100 mM NaCl at different immersion times, and the results are displayed in Fig. 7. As a reference, PVB samples were also prepared by sequentially dip-coating four individual layers of PVB on the AA2024-T3 substrate. The resulting coatings were tested by EIS under the same condition. As shown in Fig. 7a, the introduction of nanofibers into the coating matrix did not negatively affect the barrier property, which is evident by the fact that the low-frequency impedance was similar to that of PVB at the beginning of EIS measurements (Fig. 7c). This is not the case when the coated samples were prepared by a bar-coating method (Supplementary Fig. 11). During the dip-coating process, a dilute PVB solution was used, which is more likely to diffuse into the nanofiber mat and seal the interfibrillar pores. Moreover, the dilute PVB solution can lower the risk of generating artifacts that are often found by using the sticky and concentrated PVB solution during the bar-coating process. Accordingly, the resulting coated sample had fewer defects, and the embedded nanofibers did not substantially affect the barrier property of the coating matrix. However, the deterioration of the coating seems to be accelerated by the embedded nanofibers, which is supported by the larger decrease in $|Z|_{0.01\text{Hz}}$ of Fiber-PVB over time compared to that of the PVB sample (Supplementary Fig. 12). This is due to the destruction of the nanofibers with the presence of aggressive salt ions and local pH alteration during the immersion. Also, the nanofibers undesirably enhance the hydrophilicity of the coating, so the water ingress is speeded up. Since the electrolyte is easier to breach the coating, corrosion occurs more readily on the metal substrate. Unlike Fiber-PVB, Ce-Fiber-PVB showed promising corrosion resistance. In the Bode phase plot, only one time constant is observed, which is related to the coating property. The capacitive region extends towards the lower frequency over time, indicating high corrosion resistance of Ce-Fiber-PVB sample throughout the immersion (Fig. 7b). The EIS spectra acquired from Fiber-PVB and Ce-Fiber-PVB were also fitted by using the equivalent circuits with two time constants and one time constant, respectively (Supplementary Fig. 8). Only R_{pore} and C_{coat} of these two coating samples were investigated as Ce-Fiber-PVB had just one time constant characterizing the coating property, and the results are illuminated in Fig. 8 and Supplementary Fig. 13. For Fiber-PVB, R_{pore} steadily reduced from $3.4 \times 10^5 \text{ ohm cm}^2$ to $2.0 \times 10^3 \text{ ohm cm}^2$, on account of the solution absorption and the rupture of nanofibers. In the replicate EIS test, R_{pore} slightly increased when the immersion time was longer than 25 h (Fig. 8), which was possibly related to the poor protection from corrosion products. Nonetheless, it is safe to conclude that Fiber-PVB coating did not provide a sufficient degree of protection toward the AA2024-T3 substrate. On the other hand, an increase in R_{pore} of Ce-Fiber-PVB was shown because of additional corrosion protection of $\text{Ce}(\text{NO}_3)_3$ stored in the nanofibers. Additionally, C_{coat} of Ce-Fiber-PVB remained at around $1 \times 10^{-9} \text{ F cm}^{-2}$ and was always lower than that of Fiber-PVB during the immersion period

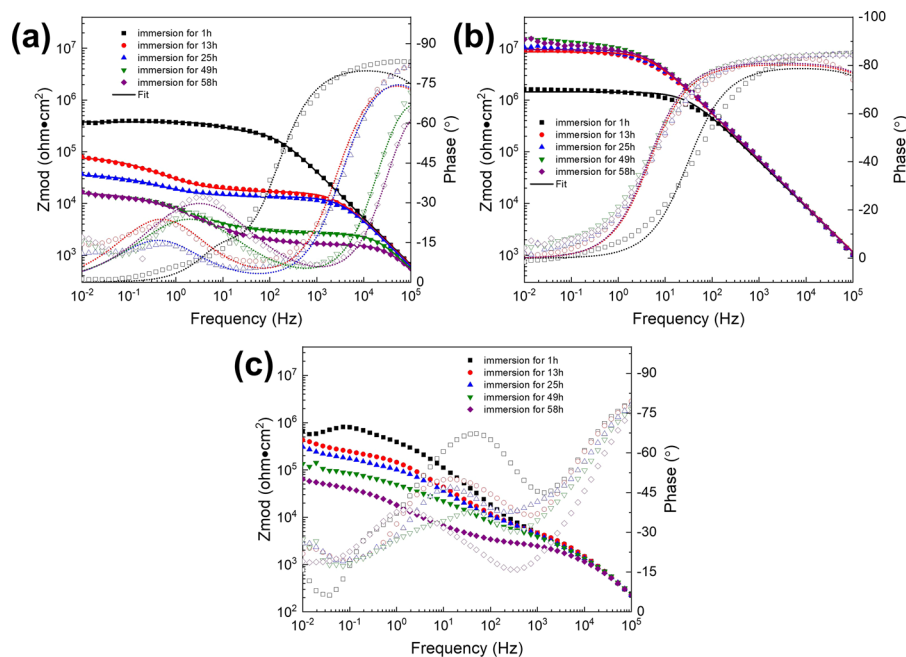


Fig. 7 EIS measurements in 100 mM NaCl. Three coated samples, including **a** Fiber-PVB, **b** Ce-Fiber-PVB, and **c** PVB, were corroded in 100 mM NaCl.

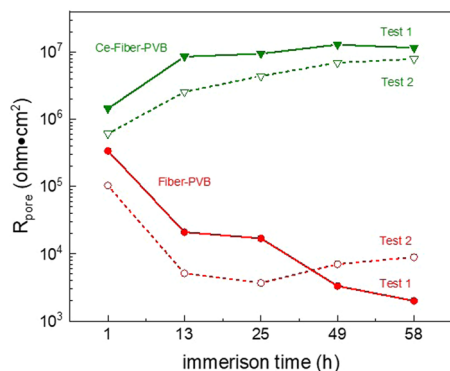


Fig. 8 Evolution of R_{pore} of coated samples. Fiber-PVB and Ce-Fiber-PVB were immersed in 100 mM NaCl.

(Supplementary Fig. 13). This again proves that the addition of Ce(NO_3)₃-loaded nanofibers can accomplish satisfying corrosion protection performance. Although changes in the coating thickness or structure inner part of the coating after EIS tests were not inspected, based on the SEM images of the surface morphology of the nanofibers after a release study (Fig. 2b), it does appear that the nanofibers were destroyed to some extent and released the entrapped Ce(NO_3)₃ during corrosion of AA2024-T3. Hence, the released Ce(NO_3)₃ enhanced the corrosion resistance of the metal substrate.

Scribe protection by Ce(NO_3)₃-loaded nanofibers

EIS measurements were conducted and the variation of $|Z|_{0.01\text{Hz}}$ with time was documented to inspect the scribe protection of the sample with Ce(NO_3)₃-loaded nanofibers. In comparison, the coating system containing Ce(NO_3)₃-loaded microspheres was also fabricated and tested under the same condition. To assure that a similar amount of corrosion inhibitors was encapsulated within the microspheres or the nanofibers, the time for the electrospay or electrospinning process was the same. The nanofibers or microspheres were then introduced into an epoxy

coating rather than a PVB coating because the epoxy coating has a superior physical barrier property and long durability. Therefore, it is assumed that the resulting coating will prevent the penetration of electrolyte and fully isolate the underlying metal substrate from the corrosive environment during 2 days of immersion if no damage is made in the coating on purpose. When an artificial scratch was made in the coating to expose the shiny metal substrate underneath, corrosion is presumed to happen in that damaged area with no corrosion in areas where the coating is not scratched. As shown in Fig. 9a, a relatively high $|Z|_{0.01\text{Hz}}$ value of approximately 8.0×10^5 ohm was measured on the freshly scribed sample with Ce(NO_3)₃-loaded microspheres, probably due to the accumulation of coating debris or corrosion products on the metal surface. The $|Z|_{0.01\text{Hz}}$ value remarkably declined to 1.3×10^5 ohm after 1.5 h, indicating corrosion of AA2024-T3. Then, the bare metal substrate was protected by the released Ce(NO_3)₃ from the microspheres located in this defect area, so $|Z|_{0.01\text{Hz}}$ recovered to 6.0×10^5 ohm. However, Ce(NO_3)₃ in this area was not abundant to offer the substrate protection against the continuous corrosion attack, thus the $|Z|_{0.01\text{Hz}}$ decreased after 3.5 h. Subsequently, a fresh scratch was made again at the same defective region to expose the underlying metal substrate after 18 h of immersion. After the second scribe was made, the corrosion resistance of the coated sample reduced and never covered again. This is likely because Ce(NO_3)₃ is quickly consumed during the first corrosion process, and corrosion inhibitors preserved in other locations of the coating cannot migrate fast enough to heal the defective zone when corrosion recurs. The same issue has been reported by numerous studies, which is generally described as limited chemical throwing power of corrosion inhibitors^{68,69} A similar result was seen in the replicate test (Supplementary Fig. 14a), where the corrosion protection could only last for a few hours. On the other hand, $|Z|_{0.01\text{Hz}}$ progressively increased from 5.0×10^5 ohm to 2.4×10^6 ohm during the first 18 h immersion for the coating sample with Ce(NO_3)₃-loaded nanofibers. Although $|Z|_{0.01\text{Hz}}$ exhibited a sudden drop to 4.0×10^4 ohm at around 12 h immersion due to the re-occurrence of corrosion, it went back to a value above 2.1×10^6 ohm after this stage. When the coating was scratched again to uncover the metal substrate, $|Z|_{0.01\text{Hz}}$ continued to increase and

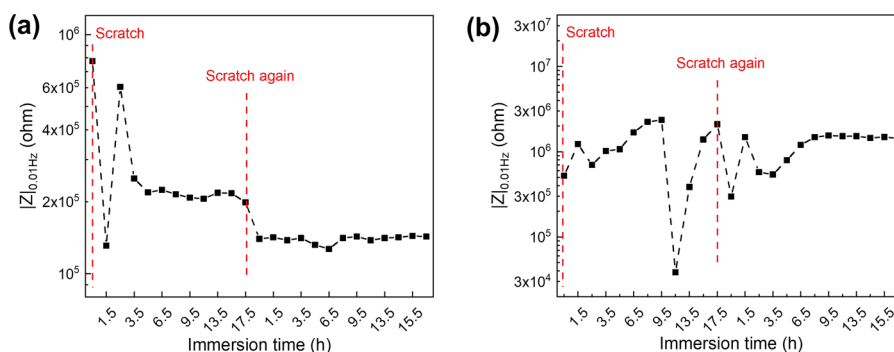


Fig. 9 EIS measurements on scratched coated samples. Evolution of $|Z|_{0.01\text{Hz}}$ of the scratched epoxy coating containing **a** $\text{Ce}(\text{NO}_3)_3$ -loaded microspheres and **b** $\text{Ce}(\text{NO}_3)_3$ -loaded nanofibers. The coated samples were immersed in 100 mM NaCl.

reach a value of 1.6×10^6 ohm (Fig. 9b). This repeatedly healing phenomenon is also observed in the replicated EIS test (Supplementary Fig. 14b). All these results suggest that the substrate could be continuously healed by the released corrosion inhibitors from the nanofibers. Unlike the inhibitor-loaded microspheres, the nanofibers can serve as a pathway for the inhibitors to be transported from other locations to the corrosion-active region, therefore, adequate corrosion inhibitors can form a stable film to prevent the re-occurrence of corrosion. This difference shown in Fig. 9a, b clearly demonstrates the effectiveness and benefit of using a fibrous delivery system to attain a repeated healing ability for long-term corrosion protection of AA2024-T3.

METHODS

Materials

Chitosan (with a medium molecular weight and deacetylation degree of 75–85%), PAA ($M_w = 450,000 \text{ g mol}^{-1}$), and rhodamine B base were purchased from Sigma-Aldrich. Formic acid, Hoechst 33258 pentahydrate, and cerium(III) nitrate hexahydrate were obtained from Fisher Scientific. PVB was ordered from Pfaltz & Bauer, and acetic acid glacial was purchased from Mallinkrodt AR. All aqueous solutions were made using deionized (DI) water with a resistivity of $18.2 \text{ M}\Omega \cdot \text{cm}$ from a Milli-Q filtration system. Aluminum alloy 2024-T3 substrates were abraded using SiC papers from 240 up to 1200 grit with ethanol as a lubricant.

Preparation of organic dye-loaded coatings

Chitosan 1.5 wt% and 12 wt% PAA solutions were prepared in 60% aqueous formic acid and 90% aqueous acetic acid, respectively, following approaches described in the literature²⁸. Both chitosan and PAA solutions were continuously stirred overnight at 50°C , and then the chitosan/PAA coacervate was prepared by adding the PAA solution into the chitosan solution dropwise while stirring until achieving a chitosan:PAA volume ratio of 2:1. To prepare organic dye-loaded coating samples, a glass slide was first dip-coated with one layer of chitosan/PAA polyelectrolyte coacervate, followed by immersion in BB solution three times with ethanol as the solvent. The subsequent deposition of five layers of the chitosan/PAA coacervate was performed by immersing the glass slide into the coacervate solution five times for a complete enclosure of organic dye (Supplementary Fig. 15a). The duration for each immersion step was 10 s. The resulting organic dye-loaded coated sample was denoted as (BB)₃/(chitosan/PAA)₅.

Release study of BB and surface morphology of coatings

To investigate the release behavior of BB from the chitosan/PAA coacervate, (BB)₃/(chitosan/PAA)₅ coated glass slides ($40 \times 25 \text{ mm}$) were immersed in 10 mL of DI water for 24 h. The pH of DI water was adjusted by 0.1 M H_2SO_4 or NaOH to pH 2.5, 7, or 10. After 24 h of immersion, the released media were collected, and the color of the released media was recorded by optical photography. To study the surface morphology of coatings, only five layers of the chitosan/PAA coacervate were dip-coated on silicon wafers that were then immersed in DI water with various pH (i.e.

pH 2.5, 7, and 10) for 24 h. The morphology of the coatings before and after immersion was examined by optical microscopy.

Fabrication of $\text{Ce}(\text{NO}_3)_3$ -loaded nanofibers

The $\text{Ce}(\text{NO}_3)_3$ -loaded nanofibers were obtained by a coaxial electrospinning technique (Supplementary Fig. 15b). The chitosan/PAA coacervate solution and 0.5 M $\text{Ce}(\text{NO}_3)_3$ dissolved in acetone were used as the shell and core liquids, respectively. The solutions were fed through a coaxial nozzle consisting of two concentrically arranged needles. A potential of 15 kV was applied on the tip of the nozzle. The nozzle-to-collector distance was 20 cm. The diameters of the inner and outer needles were 0.64 and 1.02 mm, respectively. The injection rates of the core and shell solutions were 0.2 and 1.0 mL/h, respectively. The $\text{Ce}(\text{NO}_3)_3$ -loaded nanofibers were collected on a grounded plate and then dried in an oven at 100°C for 1 h to eliminate the residual solvents. As reported previously, the change of electrospinning parameters, e.g., the applied potential, the injection rate, and humidity, may determine the properties of as-spun nanofibers^{70–72}. However, optimization of the properties of nanofibers by adjusting the operating parameters was not performed in this study.

Characterization of $\text{Ce}(\text{NO}_3)_3$ -loaded nanofibers

The morphology and composition of the $\text{Ce}(\text{NO}_3)_3$ -loaded nanofibers were examined by a ThermoFisher Apreo Field Emission SEM equipped with an EDAX Octane Elect Plus EDS detector under an acceleration voltage of 5 kV. SEM was performed in Mode 2 (Optiplan) using the standard Everhart Thornley Detector (ETD), whereas EDS was conducted in a point analysis mode. To reveal the core-shell structure of the nanofibers, confocal spectroscopy (Olympus FV1000 Filter Confocal System) and TEM (FEI Tecnai G2 Biotwin System) were utilized. To achieve fluorescent signals for confocal spectroscopic analysis, the shell solution with Hoechst 33258 pentahydrate and the core solution with rhodamine B base were simultaneously electrospun during the electrospinning process, and the as-spun nanofibers were collected on a glass slide. Subsequently, the core-shell structure was inspected by confocal spectroscopy with a laser excitation wavelength of 544 nm for rhodamine B base and 355 nm for Hoechst 33258 pentahydrate, respectively. For TEM observation, the as-spun nanofibers were directly deposited onto a 200-mesh carbon-coated Cu grid and then examined by TEM to discriminate the core and shell regions of the nanofibers.

Release study of Ce(III) from $\text{Ce}(\text{NO}_3)_3$ -loaded nanofibers

The release of Ce(III) from $\text{Ce}(\text{NO}_3)_3$ -loaded nanofibers was assessed by measuring the amount of released Ce(III) at specific time intervals with UV-vis spectroscopy at $\lambda_{\text{max}} = 250 \text{ nm}$ ^{9,73,74}. Typically, $\text{Ce}(\text{NO}_3)_3$ -loaded nanofibers were electrospun on glass slides for 1 h. The nanofibers coated glass slides were then immersed in 10 mL of DI water with pH 2.5, 7, or 10, adjusted by 0.1 M H_2SO_4 or NaOH solutions. At each sampling time, a 4 mL aliquot was extracted from the release medium for UV-vis analysis and replaced with an equivalent volume of fresh DI water with the same pH. The amount of released Ce(III) in the withdrawn solution was extrapolated from a calibration curve and the cumulative concentration of released Ce(III) was plotted as a function of time. For the release study at each pH condition, three independent measurements were performed to ensure reproducibility.

The effect of nanofibers on the integrity of coatings

Two coating formulas derived from embedding Ce(NO₃)₃-loaded nanofibers or Ce(NO₃)₃-loaded microspheres in a PVB coating matrix were used to evaluate the influence of the additive on the protective property of the coating matrix. The fabrication procedure of electrospun Ce(NO₃)₃-loaded nanofibers is presented above, while the fabrication of Ce(NO₃)₃-loaded microspheres by a coaxial electrospay method is documented in our previous publication. The size of the resulting microspheres was within 10 μm. To introduce Ce(NO₃)₃-loaded nanofibers or microspheres into the PVB coating matrix, the nanofibers or microspheres were directly deposited onto PVB bar-coated AA2024-T3 substrates during the electrospinning or the electrospaying process. Then another 3 layers of PVB were bar-coated to fully cover the nanofibers or the microspheres. The coated samples with a sandwich structure were obtained and subjected to EIS measurements in 100 mM NaCl with a neutral pH. The EIS tests were carried out using a Gamry™ Reference 600 potentiostat with a frequency range of 10⁵ Hz to 0.01 Hz. A three-electrode cell was used, consisting of a saturated calomel reference electrode (SCE), a platinum mesh counter electrode, and the coated substrate as a working electrode with an exposed area of 1 cm². After allowing the open circuit potential (OCP) to stabilize for 1 h, EIS spectra were recorded at the OCP with a 10 mV sinusoidal perturbation. However, most coating samples in this work were prepared by a dip-coating method, which is described in the following section. To conserve space, the resulting EIS data (Supplementary Fig. 11) and the corresponding discussion (see Supplementary Discussion) are provided in the Supplementary Materials.

Surface morphology of pH-sensitive coatings and EIS tests

pH-sensitive coatings were prepared using a manually dip-coating method and the substrate was vertically withdrawn from the coating solution at a speed of around 40 mm/s. Briefly, an AA2024-T3 substrate was firstly immersed in 1.25 wt% PVB ethanol solution for 10 s and then used as a collector to gather Ce(NO₃)₃-loaded nanofibers during the electrospinning process for 1 h. After drying the nanofibers in the oven at 100 °C for 1 h, the sample was immersed in PVB for 10 s three times to deposit three layers of PVB on top of the nanofibers. The resulted coating was denoted as Ce-Fiber-PVB. As a reference, nanofibers without Ce(NO₃)₃ were prepared by electrospinning the chitosan/PAA coacervate solution and acetone as the shell and core liquids, respectively. Then the inhibitor-free nanofibers were incorporated into the PVB coating with the same procedure, and the coating was named Fiber-PVB. The surface morphology of both coating samples was explored by SEM. Moreover, four individual layers of PVB were sequentially dip-coated on AA2024-T3 and the surface morphology was recorded by SEM as a control. The thickness of Ce-Fiber-PVB, Fiber-PVB, and PVB was measured by a micrometer. To inspect the protectiveness of Ce-Fiber-PVB and Fiber-PVB, EIS measurements were conducted on these coated samples after acquiring the OCP for 1 h in two sets of electrolyte solutions: 100 mM NaCl with neutral pH and 5 mM Na₂SO₄ with pH 2.5, 7, or 10 adjusted by 0.1 M H₂SO₄ or NaOH. 100 mM NaCl solution was used to investigate the corrosion protection performance of coated samples in a corrosive environment, whereas Na₂SO₄ with various pH was chosen to evaluate the protective ability of coating samples under environments undergoing anodic and cathodic reactions during metal corrosion.

Scribe protection of coating with nanofibers

To investigate if the Ce(NO₃)₃-loaded nanofibers can protect the metal substrate against corrosion repeatedly, the electrospun nanofibers were deposited on an AA2024-T3 substrate bar-coated with a single layer of PVB, followed by being fully dried in an oven at 100 °C for 1 h. Epoxy resin (EpoThin™ 2 No. 20-3440) and hardener (EpoThin™ 2 No. 20-3442) with a mass ratio of 100:45 were mixed, and the mixture was applied on top of the nanofibers with a brush. After being cured overnight at room temperature, a typical coating sample was obtained. An artificial scratch with a length of 1 cm was created on the coating by a diamond scribe and thus the underlying metal substrate was exposed. The diameter of the diamond tip is approximately 0.5 mm. Subsequently, the sample was immersed in 100 mM NaCl with a neutral pH, and the impedance was repeatedly measured for 18 h. The volume of NaCl solution was approximately 70 mL. Before each EIS measurement, the OCP was stabilized for 30 min. After 18 h of immersion, the coating samples were removed from the solution, and the same location was re-scribed to re-expose the bare metal. Then the scratched

coating samples were immersed in 100 mM NaCl solution again for the following EIS tests. In comparison, another coated sample based on the encapsulation of Ce(NO₃)₃-loaded microspheres was prepared and tested in the same way to assess its repeated self-healing performance. The fabrication of Ce(NO₃)₃-loaded microspheres was described in the previous work⁷⁵.

DATA AVAILABILITY

The data presented in this article is available upon request to the authors.

Received: 10 July 2021; Accepted: 10 October 2021;

Published online: 04 November 2021

REFERENCES

- Elangovan, K. & Balasubramanian, V. Influences of tool pin profile and tool shoulder diameter on the formation of friction stir processing zone in AA6061 aluminium alloy. *Mater. Des.* **29**, 362–373 (2008).
- Liu, Y. et al. Protective Film Formation on AA2024-T3 Aluminum Alloy by Leaching of Lithium Carbonate from an Organic Coating. *J. Electrochem. Soc.* **163**, C45–C53 (2016).
- Williams, G., Coleman, A. J. & McMurray, H. N. Inhibition of Aluminium Alloy AA2024-T3 pitting corrosion by copper complexing compounds. *Electrochim. Acta* **55**, 5947–5958 (2010).
- Prosek, T. & Thierry, D. A model for the release of chromate from organic coatings. *Prog. Org. Coat.* **49**, 209–217 (2004).
- Visser, P., Liu, Y., Terry, H. & Mol, J. M. C. Lithium salts as leachable corrosion inhibitors and potential replacement for hexavalent chromium in organic coatings for the protection of aluminum alloys. *J. Coat. Technol. Res.* **13**, 557–566 (2016).
- Shi, H. et al. Cerium cinnamate as an environmentally benign inhibitor pigment for epoxy coatings on AA 2024-T3. *Prog. Org. Coat.* **77**, 765–773 (2014).
- Thai, T. T., Trinh, A. T. & Olivier, M. G. Hybrid sol-gel coatings doped with cerium nanocontainers for active corrosion protection of AA2024. *Prog. Org. Coat.* **138**, 105428 (2020).
- Trabelsi, W., Cecilio, P., Ferreira, M. G. S. & Montemor, M. F. Electrochemical assessment of the self-healing properties of Ce-doped silane solutions for the pre-treatment of galvanised steel substrates. *Prog. Org. Coat.* **54**, 276–284 (2005).
- Abdolah Zadeh, M., Tedim, J., Zheludkevich, M., van der Zwaag, S. & Garcia, S. J. Synergetic active corrosion protection of AA2024-T3 by 2D- anionic and 3D-cationic nanocontainers loaded with Ce and mercaptobenzothiazole. *Corros. Sci.* **135**, 35–45 (2018).
- Zheludkevich, M. L. et al. Nanostructured sol-gel coatings doped with cerium nitrate as pre-treatments for AA2024-T3 Corrosion protection performance. *Electrochim. Acta* **51**, 208–217 (2005).
- Guo, X., Hurley, B. & Buchheit, R. G. Encapsulation of NaVO₃ as corrosion inhibitor into microparticles and its active corrosion protection for AA2024 based upon inhibitor control release. *Corrosion* **71**, 1411–1413 (2015).
- Zhao, X. et al. Fabrication of composite coatings with core-shell nanofibers and their mechanical properties, anticorrosive performance, and mechanism in seawater. *Prog. Org. Coat.* **149**, 105893 (2020).
- Ji, X. et al. pH-responsible self-healing performance of coating with dual-action core-shell electrospun fibers. *J. Taiwan Inst. Chem. Eng.* **104**, 227–239 (2019).
- Dieleman, C. D., Denissen, P. J. & Garcia, S. J. Long-term active corrosion protection of damaged coated-AA2024-T3 by embedded electrospun inhibiting nanonetworks. *Adv. Mater. Interfaces* **5**, 1800176 (2018).
- An, S. et al. Highly flexible transparent self-healing composite based on electrospun core-shell nanofibers produced by coaxial electrospinning for anti-corrosion and electrical insulation. *Nanoscale* **7**, 17778–17785 (2015).
- Salaluk, S. et al. Nanonetwork composite coating for sensing and corrosion inhibition. *Adv. Mater. Interfaces* **7**, 2001073 (2020).
- Demir, M. M., Horzum, N., Taşdemirci, A., Turan, K. & Güden, M. Mechanical interlocking between porous electrospun polystyrene fibers and an epoxy matrix. *ACS Appl. Mater. Interfaces* **6**, 21901–21905 (2014).
- Dong, Y., Li, S. & Zhou, Q. Self-healing capability of inhibitor-encapsulating polyvinyl alcohol/polyvinylidene fluoride coaxial nanofibers loaded in epoxy resin coatings. *Prog. Org. Coat.* **120**, 49–57 (2018).
- Yabuki, A., Kawashima, A. & Fathona, I. W. Self-healing polymer coatings with cellulose nanofibers served as pathways for the release of a corrosion inhibitor. *Corros. Sci.* **85**, 141–146 (2014).
- Therriault, D., Shepherd, R. F., White, S. R. & Lewis, J. A. Fugitive inks for direct-write assembly of three-dimensional microvascular networks. *Adv. Mater.* **17**, 395–399 (2005).

21. Toohey, K. S., Sottos, N. R. & White, S. R. Characterization of microvascular-based self-healing coatings. *Exp. Mech.* **49**, 707–717 (2009).
22. Kloet, J. Vander, Schmidt, W., Hassel, A. W. & Stratmann, M. The role of chromate in filiform corrosion inhibition. *Electrochim. Acta* **48**, 1211–1222 (2003).
23. Snihirova, D. et al. Hydroxyapatite microparticles as feedback-active reservoirs of corrosion inhibitors. *ACS Appl. Mater. Interfaces* **2**, 3011–3022 (2010).
24. Firouzi, A. et al. Electrospun protective self-healing coatings for light alloys: A better understanding of the intrinsic potential of the technology. *J. Appl. Polym. Sci.* **132**, 42728 (2015).
25. Yabuki, A., Shiraiwa, T. & Fathona, I. W. pH-controlled self-healing polymer coatings with cellulose nanofibers providing an effective release of corrosion inhibitor. *Corros. Sci.* **103**, 117–123 (2016).
26. Yabuki, A., Kanagaki, M., Nishikawa, C., Lee, J. H. & Fathona, I. W. Effective release of corrosion inhibitor by cellulose nanofibers and zeolite particles in self-healing coatings for corrosion protection. *Prog. Org. Coat.* **154**, 300–9440 (2021).
27. Pirhady Tavandashti, N. et al. PH responsive Ce(III) loaded polyaniline nanofibers for self-healing corrosion protection of AA2024-T3. *Prog. Org. Coat.* **99**, 197–209 (2016).
28. Zhang, R. Y., Zaslavski, E., Vasilyev, G., Boas, M. & Zussman, E. Tunable pH-Responsive Chitosan-Poly(acrylic acid) Electrospun Fibers. *Biomacromolecules* **19**, 588–595 (2018).
29. Li, C., Gu, Y. & Zacharia, N. S. Tuning wet adhesion of weak polyelectrolyte multilayers. *ACS Appl. Mater. Interfaces* **10**, 7401–7412 (2018).
30. Li, C., Guo, X. & Frankel, G. S. Corrosion inhibition of AA2024-T3 by smart polyelectrolyte coacervates responsive to both acidic and alkaline environments. *Prog. Org. Coat.* **146**, 105719 (2020).
31. Zhang, H., Wang, C., Zhu, G. & Zacharia, N. S. Self-healing of bulk polyelectrolyte complex material as a function of pH and salt. *ACS Appl. Mater. Interfaces* **8**, 26258–26265 (2016).
32. Udoh, I. I., Shi, H., Liu, F. & Han, E. H. Microcontainer-based waterborne epoxy coatings for AA2024-T3: Effect of nature and number of polyelectrolyte multilayers on active protection performance. *Mater. Chem. Phys.* **241**, 122404 (2020).
33. Nam, S. Y. & Lee, Y. M. Pervaporation and properties of chitosan-poly(acrylic acid) complex membranes. *J. Memb. Sci.* **135**, 161–171 (1997).
34. Rodič, P. & Milošev, I. The influence of additional salts on corrosion inhibition by cerium(III) acetate in the protection of AA7075-T6 in chloride solution. *Corros. Sci.* **149**, 108–122 (2019).
35. Lyberatos, G. & Kobotiatzi, L. Inhibition of Aluminum 7075 Alloy Corrosion by the Concerted Action of Nitrate and Oxalate Salts. *Corrosion* **47**, 820–824 (1991).
36. Williams, G. & McMurray, H. N. Anion-exchange inhibition of filiform corrosion on organic coated AA2024-T3 aluminum alloy by hydroxalate-like pigments. *Electrochim. Solid-State Lett.* **6**, 9–12 (2003).
37. Hughes, A. E., Taylor, R. J., Hinton, B. R. W. & Wilson, L. XPS and SEM characterization of hydrated cerium oxide conversion coatings. *Surf. Interface Anal.* **23**, 540–550 (1995).
38. Hinton, B. R. W. Corrosion inhibition with rare earth metal salts. *J. Alloy. Compd.* **180**, 15–25 (1992).
39. Boas, M., Grady, A., Vasilyev, G., Burman, M. & Zussman, E. Electrospinning polyelectrolyte complexes: PH-responsive fibers. *Soft Matter* **11**, 1739–1747 (2015).
40. Silva, C. L., Pereira, J. C., Ramalho, A., Pais, A. A. C. C. & Sousa, J. J. S. Films based on chitosan polyelectrolyte complexes for skin drug delivery: Development and characterization. *J. Memb. Sci.* **320**, 268–279 (2008).
41. Petrov, A. I., Antipov, A. A. & Sukhorukov, G. B. Base-acid equilibria in polyelectrolyte systems: From weak polyelectrolytes to interpolyelectrolyte complexes and multilayered polyelectrolyte shells. *Macromolecules* **36**, 10079–10086 (2003).
42. Pakravan, M., Heuzey, M. C. & Aiji, A. Core-shell structured PEO-chitosan nanofibers by coaxial electrospinning. *Biomacromolecules* **13**, 412–421 (2012).
43. Duan, B., Dong, C., Yuan, X. & Yao, K. Electrospinning of chitosan solutions in acetic acid with poly(ethylene oxide). *J. Biomater. Sci. Polym. Ed.* **15**, 797–811 (2004).
44. Core-Shell Structured PEO-Chitosan Nanofibers by Coaxial Electrospinning. *Biomacromolecules* **13**, 412–421 (2012).
45. Valero-Gómez, A., Molina, J., Pradas, S., López-Tendero, M. J. & Bosch, F. Microencapsulation of cerium and its application in sol-gel coatings for the corrosion protection of aluminum alloy AA2024. *J. Sol-Gel Sci. Technol.* **93**, 36–51 (2020).
46. Wu, J., Shaw, C. M. & Martin, D. C. Electron microscopy of organic materials: an overview and review of recent developments. *Polym. Sci. A Compr. Ref. 10 Vol. Set.* **2**, 509–525 (2012).
47. Xu, Q., Li, Y., Feng, W. & Yuan, X. Fabrication and electrochemical properties of polyvinyl alcohol/poly(3,4-ethylenedioxythiophene) ultrafine fibers via electrospinning of EDOT monomers with subsequent in situ polymerization. *Synth. Met.* **160**, 88–93 (2010).
48. Zhang, Y., Huang, Z. M., Xu, X., Lim, C. T. & Ramakrishna, S. Preparation of core-shell structured PCL-r-gelatin bi-component nanofibers by coaxial electrospinning. *Chem. Mater.* **16**, 3406–3409 (2004).
49. Reneker, D. H., Yarin, A. L., Fong, H. & Koombhongse, S. Bending instability of electrically charged liquid jets of polymer solutions in electrospinning. *J. Appl. Phys.* **87**, 4531–4547 (2000).
50. Zamani, M., Prabhakaran, M. P., Thian, E. S. & Ramakrishna, S. Protein encapsulated core-shell structured particles prepared by coaxial electrospinning: Investigation on material and processing variables. *Int. J. Pharm.* **473**, 134–143 (2014).
51. Huang, X. & Brazel, C. S. On the importance and mechanisms of burst release in matrix-controlled drug delivery systems. *J. Control. Release* **73**, 121–136 (2001).
52. Yasakau, K. A., Zheludkevich, M. L., Lamaka, S. V. & Ferreira, M. G. S. Mechanism of corrosion inhibition of AA2024 by rare-earth compounds. *J. Phys. Chem. B* **110**, 5515–5528 (2006).
53. Lee, M. W. et al. Self-healing transparent core-shell nanofiber coatings for anti-corrosive protection. *J. Mater. Chem. A* **2**, 7045–7053 (2014).
54. Badawy, W. A., Al-Kharafi, F. M. & El-Azab, A. S. Electrochemical behaviour and corrosion inhibition of Al, Al-6061 and Al-Cu in neutral aqueous solutions. *Corros. Sci.* **41**, 709–727 (1999).
55. Szklarska-Smialowska, Z. Pitting corrosion of aluminum. *Corros. Sci.* **41**, 1743–1767 (1999).
56. Pirhady Tavandashti, N., Molana Almas, S. & Esmaeilzadeh, E. Corrosion protection performance of epoxy coating containing alumina/PANI nanoparticles doped with cerium nitrate inhibitor on Al-2024 substrates. *Prog. Org. Coat.* **152**, 106133 (2021).
57. Yan, R., He, W., Zhai, T. & Ma, H. Anticorrosion organic-inorganic hybrid films constructed on iron substrates using self-assembled polyacrylic acid as a functional bottom layer. *Electrochim. Acta* **295**, 942–955 (2019).
58. Calado, L. M., Taryba, M. G., Carmezim, M. J. & Montemor, M. F. Self-healing ceria-modified coating for corrosion protection of AZ31 magnesium alloy. *Corros. Sci.* **142**, 12–21 (2018).
59. Andreatta, F. et al. Localized corrosion inhibition by cerium species on clad AA2024 aluminium alloy investigated by means of electrochemical micro-cell. *Corros. Sci.* **65**, 376–386 (2012).
60. Balaskas, A. C., Curioni, M. & Thompson, G. E. Corrosion protection mechanism of 2-mercaptobenzothiazole and its potential synergistic effect with cerium ions for treatment of AA 2024-T3. *J. Electroanal. Chem.* **863**, 114081 (2020).
61. Jakab, M. A., Presuel-Moreno, F. & Scully, J. R. Critical concentrations associated with cobalt, cerium and molybdenum inhibition of AA2024-T3 corrosion: Delivery from Al-Co-Ce(MO) alloys. *Corrosion* **61**, 246–263 (2005).
62. Palanivel, V., Huang, Y. & Van Ooij, W. J. Effects of addition of corrosion inhibitors to silane films on the performance of AA2024-T3 in a 0.5 M NaCl solution. *Prog. Org. Coat.* **53**, 153–168 (2005).
63. Aldykiewicz, A. J., Davenport, A. J. & Isaacs, H. S. Studies of the formation of cerium-rich protective films using X-ray Absorption near-edge spectroscopy and rotating disk electrode methods. *J. Electrochem. Soc.* **143**, 147–154 (1996).
64. Zhu, C. et al. Synergistic effect between glutamic acid and rare earth cerium (III) as corrosion inhibitors on AA5052 aluminum alloy in neutral chloride medium. *Ion. (Kiel).* **25**, 1395–1406 (2019).
65. Bouchaud, B., Balmain, J., Bonnet, G. & Pedraza, F. PH-distribution of cerium species in aqueous systems. *J. Rare Earths* **30**, 559–562 (2012).
66. Cervera, M. F. et al. Physical stability and moisture sorption of aqueous chitosan-amylose starch films plasticized with polyols. *Eur. J. Pharm. Biopharm.* **58**, 69–76 (2004).
67. Hirschhorn, B. et al. Determination of effective capacitance and film thickness from constant-phase-element parameters. *Electrochim. Acta* **55**, 6218–6227 (2010).
68. Scully, J. R., Tailleart, N. & Presuel-Moreno, F. Tunable multifunctional corrosion-resistant metallic coatings containing rare earth elements. in *Rare Earth-Based Corrosion Inhibitors* 267–290 (Elsevier Inc., 2014).
69. Scully, J. R., Presuel-Moreno, F., Goldman, M., Kelly, R. G. & Tailleart, N. User-selectable barrier, sacrificial anode, and active corrosion inhibiting properties of Al-Co-Ce alloys for coating applications. *Corrosion* **64**, 210–229 (2008).
70. Yördem, O. S., Papila, M. & Menceloğlu, Y. Z. Effects of electrospinning parameters on polyacrylonitrile nanofiber diameter: An investigation by response surface methodology. *Mater. Des.* **29**, 34–44 (2008).
71. Thompson, C. J., Chase, G. G., Yarin, A. L. & Reneker, D. H. Effects of parameters on nanofiber diameter determined from electrospinning model. *Polym. (Guildf.).* **48**, 6913–6922 (2007).
72. Fridrikh, S. V., Yu, J. H., Brenner, M. P. & Rutledge, G. C. Controlling the fiber diameter during electrospinning. *Phys. Rev. Lett.* **90**, 4 (2003).
73. Van Soestbergen, M., Erich, S. J. F., Huinink, H. P. & Adan, O. C. G. Dissolution properties of cerium dibutylphosphate corrosion inhibitors. *Corros. Eng. Sci. Technol.* **48**, 234–240 (2013).
74. Van Soestbergen, M., Baukh, V., Erich, S. J. F., Huinink, H. P. & Adan, O. C. G. Release of cerium dibutylphosphate corrosion inhibitors from highly filled epoxy coating systems. *Prog. Org. Coat.* **77**, 1562–1568 (2014).

75. Li, C., Guo, X., Frankel, G. S. Corrosion inhibition of AA2024-T3 by a coating containing dual-pH sensitive, corrosion inhibitor loaded microspheres. *Corros. Sci.* **107**, 109835 <https://doi.org/10.1016/J.CORSCI.2021.109835> (2021).

ACKNOWLEDGEMENTS

SEM analysis was carried out at Center for Electron Microscopy and Analysis (CEMAS) at The Ohio State University, while TEM study was performed at Campus Microscopy and Imaging Facility (CMIF) at The Ohio State University.

AUTHOR CONTRIBUTIONS

The manuscript was written through contributions of all authors. C.L. and X.G.-Conceptualization; C.L.-Investigation, writing original draft; X.G.-Writing review & editing; G.S.F.-Supervision, writing review & editing.

COMPETING INTERESTS

The authors declare no competing interests.

ADDITIONAL INFORMATION

Supplementary information The online version contains supplementary material available at <https://doi.org/10.1038/s41529-021-00203-3>.

Correspondence and requests for materials should be addressed to Gerald S. Frankel.

Reprints and permission information is available at <http://www.nature.com/reprints>

Publisher's note Springer Nature remains neutral with regard to jurisdictional claims in published maps and institutional affiliations.



Open Access This article is licensed under a Creative Commons Attribution 4.0 International License, which permits use, sharing, adaptation, distribution and reproduction in any medium or format, as long as you give appropriate credit to the original author(s) and the source, provide a link to the Creative Commons license, and indicate if changes were made. The images or other third party material in this article are included in the article's Creative Commons license, unless indicated otherwise in a credit line to the material. If material is not included in the article's Creative Commons license and your intended use is not permitted by statutory regulation or exceeds the permitted use, you will need to obtain permission directly from the copyright holder. To view a copy of this license, visit <http://creativecommons.org/licenses/by/4.0/>.

© The Author(s) 2021